IN VIVO OPTICAL IMAGING OF BRAIN FUNCTION

Edited by
Ron D. Frostig

CRC PRESS

Boca Raton London New York Washington, D.C.

8 Noninvasive Imaging of Cerebral Activation with Diffuse Optical Tomography

David A. Boas, Maria Angela Franceschini, Andy K. Dunn, and Gary Strangman

CONTENTS

0-8493-2389-4/02/$0.00+$1.50

8.1 INTRODUCTION

Optical methods have been used to measure physiological variables for decades, as is apparent from other chapters in this book. However, the use of *diffuse* optical light for physiological monitoring — and for noninvasive monitoring in particular — has a somewhat shorter history. This delayed development resulted from two primary obstacles. The first obstacle was sensitivity — a need to discover a sufficiently nonabsorbing wavelength range and to develop sufficiently sensitive detectors to monitor through relatively large distances (centimeters) of tissue. As it turns out, the near-infrared wavelength range between roughly 600 and 950 nm is relatively poorly absorbed by biological tissue. Furthermore, the primary absorbers in this wavelength range are oxyhemoglobin and deoxyhemoglobin (HbO and Hb, respectively), which are important biological indicators. In the late 1970s, Jöbsis[1] was the first to use near-infrared light to measure hemodynamic parameters of the brain noninvasively. This work employed what is now called near-infrared spectroscopy (NIRS), a point-source measurement of species concentrations within tissue.

It was to be some years before actual imaging with diffuse light (diffuse optical tomography, or DOT) would appear, however, because of the second obstacle: a need for better understanding of how light propagates through highly scattering (diffusive) tissue. Considerable work has appeared on the theory of light propagation through scattering media in recent years (for a review, see Reference 2), and this work, along with phantom studies, has made imaging with diffuse light a reality.

Prior to these developments, and since Jöbsis' initial work, many groups have examined a variety of biologically relevant parameters in tissue, including brain.[3,4] Early research, during the 1980s and early 1990s, focused on the use of diffuse near-infrared light for measuring brain hemoglobin oxygen saturation within neonate and adult humans.[5-9] In the early 1990s, functional magnetic resonance imaging (fMRI) came of age, providing whole-brain imaging of the blood oxygen level–dependent (BOLD) signal associated with altered blood flow and oxygen metabolism within the brain.[10-14] Shortly after this development, NIRS was shown to reveal sensitivity similar to that of fMRI.[15-18] While sensitive to similar species, an important characteristic of the optical measure of brain activity was its ability to separately distinguish changes in oxy- and deoxyhemoglobin concentrations,[19] whereas fMRI only indirectly measures relative changes in deoxyhemoglobin.[20] NIRS has the further advantage of being inexpensive and portable, thus allowing studies of more subjects under a wider range of conditions. These advantages must, of course, be weighed against the principal limitations of the optical techniques: the current lack of anatomical imaging for localization purposes and the relatively shallow penetration depth (particularly during brain monitoring).

To date, many research groups worldwide have used NIRS in functional brain studies as a noninvasive tool to monitor local changes in cerebral oxygenation and hemodynamics.[21-33] In addition, several groups have investigated the possibility of using NIRS to measure the cytochrome oxidase (cyt-ox) redox state.[34,35] Cyt-ox oxidation is a marker of intracellular energy metabolism and has been suggested as

a possible parameter to assess the functional state of the brain.[36-40] These optical measurements are usually conducted over a wide spectral range (extending up to 500 nm), because the absorption contributions of cyt-ox are an order of magnitude (or more) smaller than those of hemoglobin.

A few groups have also worked on using diffuse light to measure neuronal activity directly rather than indirectly via hemoglobin. For example, it has been shown *in vitro* that neuronal activity is associated with an increase in light scattering, induced by a change in the index of refraction of the neuronal membranes.[41-43] Following up on this work, near-infrared optical methods have been successfully used to detect such light-scattering changes *in vivo* in adult humans.[44-46] This fast optical signal appears to show the same time course as the electrophysiological response measured with EEG or electrophysiological techniques.

Although still in its infancy, the use of diffuse light for noninvasive imaging (diffuse optical tomography, DOT) is progressing quickly.[2,47] The accumulating literature clearly demonstrates the unique ability of near-infrared techniques to detect hemodynamic, metabolic, and neuronal signals associated with brain activity. Moreover, these techniques hold promise of eventually providing absolute quantitative values for at least hemodynamic and metabolic parameters. No other single imaging modality has this ability; fMRI can measure relative hemodynamic changes, EEG and MEG can measure neuronal signals, and PET can measure blood flow, volume, and glucose metabolism.

The unique abilities of optical methods are further supplemented by the applicability of diffuse optical techniques to a variety of studies that are highly problematic for other brain-imaging techniques. Such studies include neurobehavioral development in infants and young children and functional reorganization during stroke or brain-injury rehabilitation, among others. This wide applicability motivates further development of the technology toward whole-head absolute quantitative imaging.

In the remainder of this chapter, we review the basic principles of NIRS and DOT, discuss example instrumentation implementations, and provide illustrative brain activation data. We then summarize with a discussion of the future directions for functional optical brain imaging.

8.2 THEORY

It is a relatively simple step, conceptually speaking at least, to move from the simple NIRS point measurement to imaging of these same variables. Before going into the details of imaging *per se*, however, we will first briefly review the physical model of photon migration through tissue that is needed to obtain quantitatively accurate estimates of the chromophore concentration changes within the brain during functional activation. We continue to make the distinction between NIRS and DOT, in which the former indicates nonimaging point measurements while the latter is reserved for imaging measurements. The distinction in instrumentation depends only on the number and arrangement of sources and detectors used for measurements. The rest of this section reviews the theoretical concepts of NIRS and DOT.

8.2.1 NIRS Theory*

The theory of the modified Beer–Lambert Law (MBLL) has been explained previously.[5,48] This technique is based on the absorption of near-infrared light by oxy- and deoxyhemoglobin. Changes in the concentrations of these chromophores are quantified using a modified Beer–Lambert law, which is an empirical description of optical attenuation in a highly scattering medium.[5,48] The modified Beer–Lambert law is

$$OD = -\log\frac{I}{I_o} = \varepsilon CLB + G \tag{8.1}$$

where OD is the optical density, I_o is the incident light intensity, I is the detected light intensity, ε is the extinction coefficient of the chromophore, C is the concentration of the chromophore, L is the distance between where the light enters the tissue and where the detected light exits the tissue, B is a pathlength factor that accounts for increases in the photon pathlength caused by tissue scattering, and G is a factor that accounts for the measurement geometry. We use the convention of log base e.

A change in the chromophore concentration causes the detected intensity to change. When the concentration changes, the extinction coefficient ε and distance L remain constant and it is assumed that B and G remain constant. Thus, Equation 8.1 can be rewritten as

$$\Delta OD = -\ln\frac{I_{Final}}{I_{Initial}} = \varepsilon \Delta CLB \tag{8.2}$$

where $\Delta OD = OD_{Final} - OD_{Initial}$ is the change in optical density (the logarithm is base e), I_{final} and $I_{Initial}$ are the measured intensities before and after the concentration change, and ΔC is the change in concentration. L is specified by the probe geometry, ε is an intrinsic property of the chromophore, and B is often referred to as the differential pathlength factor (DPF), which can be determined from independent measurements with ultra-short pulses of light[49] and has been tabulated for various tissues. Thus, given the extinction coefficient, it is possible to quantify the change in chromophore concentration.

Figure 8.1 plots the extinction coefficients for oxy- and deoxyhemoglobin vs. wavelength as measured by Wray et al., Cope, and Matcher et al.[6,48,50] The wavelength range of 700 to 950 nm is the only region in which light is able to penetrate several centimeters through tissue. The other chromophores of significance in tissue in this wavelength range are water, lipids, and cytochrome aa3. We do not consider these chromophores in this chapter, as their contribution in general is an order of

* The generalization of this formula for more than two wavelengths can be found in Cope, M., *The Development of a Near-Infrared Spectroscopy System and Its Application for Noninvasive Monitoring of Cerebral Blood and Tissue Oxygenation in the Newborn Infant,* University College, London, 1991.

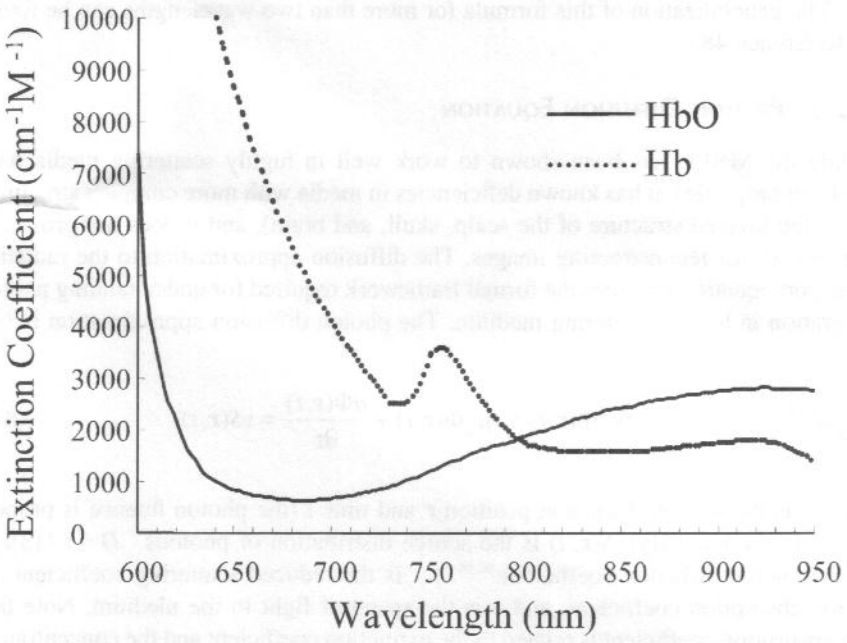

FIGURE 8.1 Absorption spectrum of oxyhemoglobin (HbO) and deoxyhemoglobin (Hb). Below 600 nm the absorption increases by more than a factor of 10, while above 950 nm water absorption increases significantly.

magnitude less significant than hemoglobin and is not easily measured without use of six or more wavelengths. In order to consider the contribution of two chromophores, we must rewrite Equation 8.2 as

$$\Delta OD^{\lambda} = (\varepsilon^{\lambda}_{\text{HbO}}\,\Delta[\text{HbO}] + \varepsilon^{\lambda}_{\text{Hb}}\,\Delta[\text{Hb}])B^{\lambda}L \tag{8.3}$$

where λ indicates a particular wavelength. Equation 8.3 explicitly accounts for independent concentration changes in oxyhemoglobin (Δ[HbO]) and deoxyhemoglobin (Δ[Hb]).

By measuring ΔOD at two wavelengths (λ_1 and λ_2) and using the known extinction coefficients of oxyhemoglobin (ε_{HbO}) and deoxyhemoglobin (ε_{Hb}) at those wavelengths, we can then determine their concentration changes:

$$\Delta[\text{Hb}] = \frac{\varepsilon^{\lambda_2}_{HbO}\dfrac{\Delta OD^{\lambda_1}}{B^{\lambda_1}} - \varepsilon^{\lambda_1}_{HbO}\dfrac{\Delta OD^{\lambda_2}}{B^{\lambda_2}}}{(\varepsilon^{\lambda_1}_{Hb}\varepsilon^{\lambda_2}_{HbO} - \varepsilon^{\lambda_2}_{Hb}\varepsilon^{\lambda_1}_{HbO})L}$$

$$\Delta[\text{HbO}] = \frac{\varepsilon^{\lambda_1}_{Hb}\dfrac{\Delta OD^{\lambda_2}}{B^{\lambda_2}} - \varepsilon^{\lambda_2}_{Hb}\dfrac{\Delta OD^{\lambda_1}}{B^{\lambda_1}}}{(\varepsilon^{\lambda_1}_{Hb}\varepsilon^{\lambda_2}_{HbO} - \varepsilon^{\lambda_2}_{Hb}\varepsilon^{\lambda_1}_{HbO})L} \tag{8.4}$$

The generalization of this formula for more than two wavelengths can be found in Reference 48.

8.2.2 Photon Diffusion Equation

While the MBLL has been shown to work well in highly scattering media with uniform properties, it has known deficiencies in media with more complex structures (e.g., the layered structure of the scalp, skull, and brain), and it does not provide a framework for reconstructing images. The diffusion approximation to the radiative transport equation provides the formal framework required for understanding photon migration in highly scattering medium. The photon diffusion approximation is[51-53]

$$-D\nabla^2\Phi(\mathbf{r},t)+v\mu_a\Phi(\mathbf{r},t)+\frac{\partial\Phi(\mathbf{r},t)}{\partial t}=vS(\mathbf{r},t) \tag{8.5}$$

$\Phi(\mathbf{r}, t)$ is the photon fluence at position $\mathbf{r}$ and time t (the photon fluence is proportional to the intensity). $S(\mathbf{r}, t)$ is the source distribution of photons. $D = v / (3\mu_s')$ is the photon diffusion coefficient,[54,55] μ_s' is the reduced scattering coefficient, μ_a is the absorption coefficient, and v is the speed of light in the medium. Note that the absorption coefficient is related to the extinction coefficient and the concentration as $\mu_a = \varepsilon C$. For a combination of the hemoglobin chromophores,

$$\mu_a=\varepsilon_{HbO}[HbO]+\varepsilon_{Hb}[Hb] \tag{8.6}$$

Equation 8.5 accurately models the migration of light through highly scattering media, provided that the probability of scattering is much greater than the absorption probability. Note that all factors in Equation 8.5 are wavelength dependent.

Solutions of the photon diffusion equation can be used to predict the photon fluence (or intensity) detected for typical diffuse measurements.[53] Assuming that concentration changes are both global and small, the solution of the photon diffusion equation for a semi-infinite medium is

$$\begin{aligned}\Delta OD &= -\log\frac{\Phi_{Final}}{\Phi_{Initial}}\\ &=\frac{1}{2}\left(\frac{3\mu_s'}{\mu_a^{Initial}}\right)^{1/2}\left[1-\frac{1}{(1+L(3\mu_s'^{\,Initial}\mu_a^{Initial})^{1/2})}\right](\varepsilon_{HbO}\Delta[\mathrm{HbO}]+\varepsilon_{Hb}\Delta[\mathrm{Hb}])L\end{aligned} \tag{8.7}$$

The solution of the photon diffusion equation for representative tissue geometry (Equation 8.7) tells us that the modified Beer–Lambert law is reasonable for tissues with spatially uniform optical properties when the chromophore concentration does not change significantly (i.e., $\Delta[X]/[X] << 1$). Equation 8.7 shows that the pathlength factor B in Equation 8.3 is given by

$$B = \frac{1}{2}\left(\frac{3\mu_s'}{\mu_a^{Initial}}\right)^{1/2}\left[1 - \frac{1}{(1 + L(3\mu_s'^{Initial}\mu_a^{Initial})^{1/2})}\right] \tag{8.8}$$

for a semi-infinite medium. This shows that B depends on tissue scattering, initial chromophore concentration, extinction coefficient (thus, B is wavelength dependent), and optode separation. In practice, the validity of the assumption that B is independent of μ_a and L has often been ignored since B is, in general, empirically determined and the changes in μ_a are typically small.

8.2.3 Diffuse Optical Tomography

The preceding equations apply to every individual measurement that might be made from a NIRS or a DOT system. In order to generate an image of spatial variations in Hb and HbO, all that we need to do is to measure the photon fluence at multiple source and detector positions (typically with overlapping sensitivities) and essentially backproject the image. The general solution of the photon diffusion equation at the detector position $\mathbf{r}_d$ for a medium with spatially varying absorption is

$$\Phi(\mathbf{r}_d) = \Phi_{incident}(\mathbf{r}_d) - \int \Phi(\mathbf{r})\frac{v}{D}(\varepsilon_{HbO}\Delta[\mathrm{HbO}] + \varepsilon_{Hb}\Delta[\mathrm{Hb}])G(\mathbf{r}, \mathbf{r}_d)d\mathbf{r} \tag{8.9}$$

For reflectance in a semi-infinite medium, the solutions for $\Phi_{incident}$ and $G(\mathbf{r}, \mathbf{r}_d)$ can be found in Farrell et al.[56] Equation 8.9 is an implicit equation for the measured fluence as $\Phi(\mathbf{r})$ appears in the integral on the right-hand side. One way to solve this equation uses the first Born approximation, which assumes that $\Phi(\mathbf{r}) = \Phi_{incident} + \Phi_{sc}$ where[57,58]

$$\Phi_{sc}(\mathbf{r}_d) = -\int \Phi_{incident}(\mathbf{r})\frac{v}{D}(\varepsilon_{HbO}\Delta[\mathrm{HbO}] + \varepsilon_{Hb}\Delta[\mathrm{Hb}])G(\mathbf{r}, \mathbf{r}_d)d\mathbf{r} \tag{8.10}$$

By measuring $\Phi_{sc}(\mathbf{r}_d)$ using multiple source and detector positions and multiple wavelengths, we can invert the integral equation to obtain images of Δ[HbO] and Δ[Hb]. There are numerous methods for solving Equation 8.10.[59] Most rely on reducing Equation 8.10 to a matrix equation by rewriting the integral as a sum over voxels; i.e., $y = Ax$ where y is the vector of measurements (i.e., $\Phi_{sc}(\mathbf{r}_d)$), x is the vector of image voxels, and A is the transformation matrix obtained from the integrand of Equation 8.10. For the case of fewer measurements than unknowns, the linear inverse problem is underdetermined and is given by the (regularized) Moore–Penrose generalized inverse

$$\hat{x} = -A^T(AA^T + \lambda I)^{-1}y \tag{8.11}$$

where I is the identity matrix and $\lambda = \alpha \max(AA^T)$ is the Tikhonov regularization parameter.

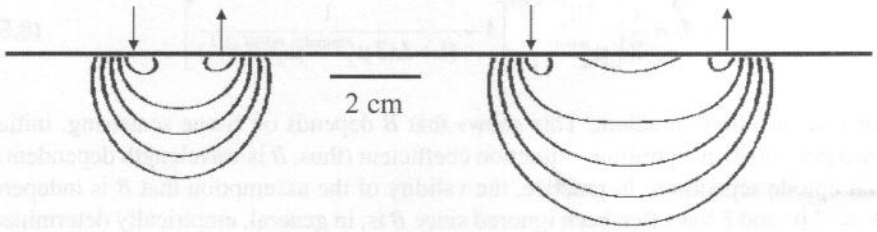

FIGURE 8.2 Photon migration sensitivity profile shown for a semi-infinite medium for 2- and 4-cm source detector separation. Contour lines are shown every half-order of magnitude.

8.2.4 DOT Simulations

Equation 8.10 describes the spatial sensitivity profile of light diffusing through a highly scattering medium. In Figure 8.2 we show the sensitivity profile for a simple reflectance geometry with a continuous-wave (CW) light source using typical tissue optical properties of $\mu_s' = 10\ cm^{-1}$ and $\mu_a = 0.1\ cm^{-1}$. The most important point is that the spatial sensitivity profile is not localized but covers a large volume and therefore intrinsically has relatively poor spatial resolution. Second, notice that as the separation between the source and detector increases, the penetration depth also increases. This fact can be used to probe deeper into the brain and possibly even to distinguish superficial scalp from deeper brain signals.

Figure 8.3 illustrates the process of reconstructing an image with diffuse light. The process is conceptually similar to that of x-ray computed tomography, which

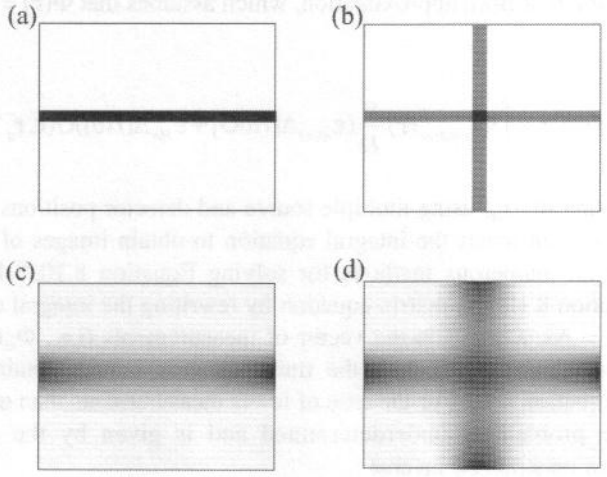

FIGURE 8.3 Comparison of x-ray computed tomography (a, b) and diffuse optical tomography (c, d) of a square absorbing object in the center of the outer square. X-ray tomography has greater resolution, as indicated by the sharper edges of the reconstructed image. Diffuse optical tomography reconstructs the object but with reduced resolution because of the diffusive nature of near-infrared photon migration in tissue.

is included for comparison. In the case of x-rays, a collimated beam transilluminates the tissue, maintaining high spatial resolution, and the attenuation of the beam is measured. The measured attenuation is then backprojected into the tissue along the axis of the x-ray. For a simple object positioned in the center of the plane, we see that a single x-ray projection sharply defines the lateral boundaries of the object but does not localize the object along the x-ray propagation axis. Through the combination of additional measurements at different angles with respect to the object, it is possible to obtain a high-resolution image of the x-ray attenuating object within the tissue. Figure 8.3b shows the result from two orthogonal projections. The artifacts near the boundaries are reduced with additional projections.

Figures 8.3c and d show the results obtained with diffuse light by following the same backprojection procedure. The striking difference obtained with a single projection is that the boundaries of the object are not sharply defined, and the object appears to be near the sources and detectors where the sensitivity of the measurement is greatest. The first observation is an intrinsic limitation of imaging with diffuse light, while the second is an artifact of the backprojection procedure. Utilizing an additional orthogonal projection (Figure 8.3d), we see better localization of the absorbing object. We note that while the backprojection method provides quantitative images with x-ray CT, it is only an approximation for DOT. This difference results from the fact that the measured diffuse light has sampled a volume of tissue, as opposed to the measured x-ray that samples only along a line through the sample. The backprojection method, therefore, does not produce an image that optimally fits the experimental data. More sophisticated optimization is needed to obtain quantitative image reconstruction with diffuse light.[2]

8.2.5 Theoretical Optical Sensitivity to the Brain

Photon migration theory models the propagation of light through tissue and enables the extraction of information about the tissue from measurements of remitted diffuse light. By using Monte Carlo techniques we can simulate the propagation of photons through tissue and obtain a spatial sensitivity map.[60-62] In such simulations, individual photon trajectories are traced by sampling appropriate probability distributions for scattering events. After 10^6 to 10^8 photons are traced, quantities such as the fraction of photons reaching a particular detector or the spatial sampling of the tissue can be determined.

In our Monte Carlo model, the tissue is a three-dimensional volume with optical properties assigned to each voxel; source and detectors can be placed at any voxel. Photons are propagated until they exit the tissue, and the total pathlength in each tissue type is recorded for all photons reaching a detector. Only recently has the computational power become widely available for the practical use of Monte Carlo simulations. (One simulation typically takes 10 to 20 h on current high-end desktop systems.)

Figure 8.4 shows an anatomical MRI of a human head, segmented into five tissue types (air, scalp, skull, cerebral spinal fluid, and gray/white matter; see Reference 63), with a contour overlay indicating the photon migration spatial sensitivity profile for (a) continuous-wave, (b) 200-MHz modulation, and (c,d) pulsed measurements. One contour line is shown for each half-order of magnitude

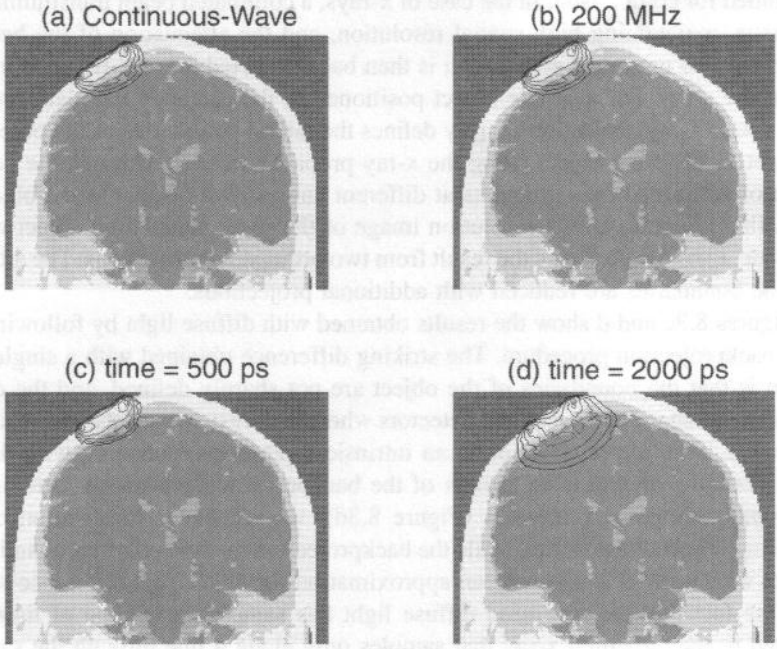

FIGURE 8.4 Contour plots of the photon migration sensitivity profile in a 3D human head as determined from Monte Carlo simulations. Details provided in the text.

(10 dB) signal loss, and the contours end after three orders of magnitude in loss (60 dB). For the 3D Monte Carlo simulation, we assumed that $\mu_s' = 10\ cm^{-1}$ and $\mu_a = 0.4\ cm^{-1}$ for the scalp and skull, $\mu_s' = 0.1\ cm^{-1}$ and $\mu_a = 0.01\ cm^{-1}$ for the CSF, and $\mu_s' = 12.5\ cm^{-1}$ and $\mu_a = 0.25\ cm^{-1}$ for the gray/white matter. Note that the contours extend several millimeters into the brain tissue, indicating sensitivity to changes in cortical optical properties. The depth-penetration difference between the continuous-wave and 200-MHz measurements is difficult to discern. A ratio of the two sensitivity profiles (not shown) shows that the 200-MHz profile is shifted slightly towards the surface. The time domain sensitivity profiles suggest the possibility of obtaining greater penetration depths in the head from measurements made at longer delay times.

8.3 INSTRUMENTATION

Several technical solutions exist for implementation of NIRS and DOT, including time domain (TD), frequency domain (FD), and continuous-wave (CW) systems. TD systems[47,64-67] introduce into tissue extremely short (picosecond) incident pulses of light that are broadened and attenuated (i.e., scattered and absorbed) by the various tissue layers such as skin, skull, cerebrospinal fluid (CSF), and brain. A TD system detects the temporal distribution of photons as they leave the tissue; the shape of this distribution provides information about tissue scattering and absorption. In FD systems,[68-71] the light source is on continuously but is amplitude modulated at

frequencies on the order of tens to hundreds of megahertz. Information about the absorption and scattering properties of tissue is obtained by recording amplitude decay and phase shift (delay) of the detected signal with respect to the incident one.[72] In CW systems,[73-76] light sources emit light continuously as FD systems do but at constant amplitude or modulated at frequencies not higher than a few tens of kilohertz. These systems measure only the amplitude decay of the incident light and therefore do not provide sufficient information to quantify baseline absorption and scattering separately.

Each of these techniques has intrinsic advantages and drawbacks. TD systems can theoretically obtain the highest spatial resolution and can accurately determine absorption and scattering. Drawbacks include long acquisition times to achieve reasonable signal-to-noise ratios, a need to mechanically stabilize the instrument, and the large dimensions and high cost of the necessary ultrafast lasers.[77] These drawbacks have limited the use of TD systems, but technological advances are beginning to make them more attractive.[78]

State-of-the-art FD systems cover a wide range of applications for clinical use and can achieve considerably higher temporal resolution than TD systems. FD instruments are typically less expensive to build than TD systems but are still more expensive than CW systems, and they require more careful engineering and optimization to eliminate noise, ground loops, and RF-transmitter effects. While they are able to measure scattering effects, the noise in such measurements remains a significant issue.

CW technology can be engineered with relatively inexpensive and widely available components; a hospital pulse oximeter is an example of the small dimensions achievable for a CW NIRS instrument. The CW's primary shortcoming compared to TD and FD systems is the inability to uniquely quantify the effects of light scattering and absorption.[79] Despite their relatively minimal design requirements, commercially available systems until recently featured only a single detector (NIRO 500; see Reference 5) or had a restricted bandwidth (2 Hz: OXYMON, University of Nijmegen, see Reference 80). We are now seeing considerable development of CW technology to greater bandwidths and greater numbers of source and detectors.[81-84]

It is likely that CW technology will quickly find widespread use among brain researchers because of its relatively low cost, portability, and ease of implementation and use compared to FD and TD systems while still displaying sensitivity to cerebral hemodynamic features. Arguably, a CW imaging system will also achieve the best signal-to-noise ratio at image frame rates faster than 1 Hz. For these reasons, we focus below on discussing basic instrument design of CW NIRS and DOT systems. While CW imaging techniques have the potential to provide quantitative images of hemodynamics changes during brain activation, quantitative imaging of baseline brain states is likely to be possible only with FD and TD methods because they provide time-delay and amplitude information.

8.3.1 NIRS Instrument

A basic NIRS system delivers light of preferably two or more wavelengths to a single position on the tissue and then collects and detects the diffusely re-emitted

light at one or more locations. Because the light must travel several centimeters through the scalp and skull to sample the adult human brain, it is necessary that light sources be chosen with sufficient power and in the wavelength range between 600 and 950 nm where light absorption is minimized. This typically requires using laser diodes, although filtered white light sources have also been successfully used in adult humans.[39] The optical power incident on the tissue must be no more than 4 mW per 1 mm^2 for safe, long-term tissue exposure to laser light.[85]

To gain sensitivity to the brain in the adult human, detectors must be placed at least 2.5 cm from the source (less for babies, due to their thinner scalps and skulls), as the depth of sensitivity is roughly proportional to the source–detector separation. With such separations, the amount of light reaching the detector is on the order of 10 pW (an attenuation of 9 decades). Therefore, to obtain a decent signal-to-noise ratio at desired bandwidths of 1 Hz or greater, it is necessary to use high-sensitivity detectors: photo-multiplier tubes (PMTs), avalanche photodiodes (APDs), or CCD cameras.

Figure 8.5 shows a photograph of our CW NIRS system. The sources in this system are two low-power laser diodes emitting light at discrete wavelengths, typically 785 nm (Sanyo, DL7140-201) and 830 nm (Hitachi, HL8325G). These lasers are powered by a stabilized current, intensity modulated by an approximately 5-kHz square wave at a 50% duty cycle. Both diodes are driven at the same frequency but phase shifted by 90° with respect to one another. This phase encoding, known as an in-phase/quadrature-phase (IQ) circuit, allows simultaneous laser operation as well as separation of the contributions of each source to a given detector's signal.

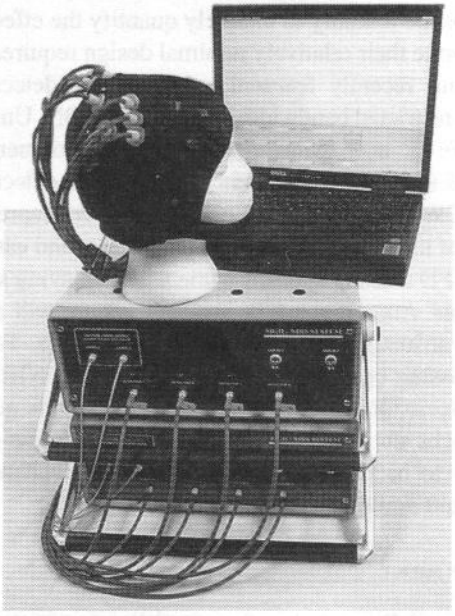

FIGURE 8.5 Photograph of the NIRS system and cap used to hold fiber optics on the head.

The system has four separate detector modules (Hamamatsu C5460-01), which are optically and electrically isolated from each other. Each module consists of a silicon avalanche photodiode (APD) with a built-in, high-speed, current-to-voltage amplifier and temperature compensation. The modules achieve a gain of typically 10^8 V/W with a noise equivalent power of 0.04 pW/(Hz)$^{-0.5}$ resulting from the high detector sensitivity. The incoming signal at a given detector is composed of both source colors, which are separated by synchronous (lock-in) detection using the two source signals as a reference. The output of the decoding portion of the IQ circuit includes two signal components, corresponding to the two laser wavelengths. These two components are low-pass filtered at 20 Hz and digitized by a computer.

8.3.2 Imaging Instrumentation

Conceptually, an imaging instrument is a simple extension of a NIRS system to include more sources and detectors. Adding more detectors is straightforward because each detector operates independently, without interaction with the other detectors. The sources, on the other hand, introduce light into the tissue and detectors can only detect the total amount of light present at a given time. Thus, in order to assign light received at a detector properly to each individual source, the source light must be encoded.

Several encoding strategies exist: time sharing, time encoding, and frequency encoding. Time sharing is the easiest to implement. In this scheme, each source is turned on, one at a time, long enough for the detectors to acquire a decent signal (typically 10 to 100 msec). Large numbers of sources give rise to slow image frame rates and temporal skew between sources. Time encoding overcomes the temporal skew problem by switching between sources at a much faster rate (100 μsec or faster) but integrating the signal from each source over several switch cycles (e.g., the same 10 to 100 msec) and resulting in roughly the same image frame rate as with time sharing. Finally, frequency encoding turns all sources on at the same time but modulates the intensity of each one at a slightly different frequency. The individual source signals are then discriminated at the detector by employing simple analog or digital band-pass filters at the frequencies of source modulation. While the duty cycle in this scheme is maximized, the effective dynamic range of the system is limited by the fact that all sources are on at the same time. That is, it can be difficult to detect a distant source several orders of magnitude weaker than a source close by, given that each detector has a fixed dynamic range (typically three to four orders of magnitude).

Figure 8.6 shows a block diagram and photograph of our DOT imaging system with 18 lasers and 16 detectors. This system is being extended to 32 lasers (intensities driven at 32 different frequencies) and 32 detectors. At present, the 18 lasers are divided into 9 lasers at 785 nm (Sanyo, DL7140-201) and 9 lasers at 830 nm (Hitachi, HL8325G), although they can be divided among as many different wavelengths as desired. The detectors are avalanche photodiodes (APDs, Hamamatsu C5460-01). A master clock generates the 18 distinct frequencies between 4.0 and 7.4 kHz in approximately 200-Hz steps. These frequencies are then used to drive the individual lasers with current stabilized square-wave modulation. Following each APD module

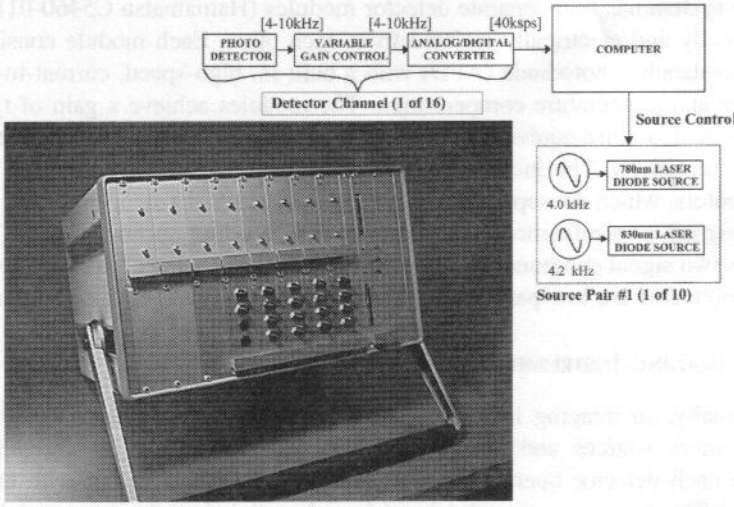

FIGURE 8.6 Photograph and block diagram of the frequency-encoded, continuous-wave diffuse optical tomography system. Details provided in the text.

is a bandpass filter with a cut-on frequency of ~500 Hz to reduce 1/f noise and the 60-Hz room light signal and a cut-off frequency of ~10 kHz to reduce the third harmonics of the square-wave signals. After the bandpass filter is a programmable gain stage to match the signal levels with the acquisition level on the analog-to-digital converter within the computer. Each detector is digitized at ~40 kHz and the individual source signals are then obtained by use of a digital bandpass filter — for example, a discrete Fourier transform or an infinite impulse–response filter.

8.4 NIRS AND DOT EXPERIMENTS

8.4.1 NIRS DOT Paradigm

To demonstrate that such an instrument has the ability to measure cerebral hemodynamic signals in humans noninvasively, we conducted simple experiments with young, healthy volunteers. A basic motor protocol was chosen to investigate the recordability of optical signals from the brain and to allow comparison with validated findings of deoxyhemoglobin and volume changes found in fMRI studies. Either two NIRS systems were used in parallel to record time-locked signals from two separate but broad regions of the brain or our newer DOT imaging system was used. In the NIRS experiments, the multiple detectors were used primarily to simplify the localization process. All subjects consented to the experimental procedure, which was approved by the Massachusetts General Hospital institutional review board.

The positions of the optodes were separately determined for each paradigm so as to cover an area over the cortex activated by similar fMRI studies.[11,86-89] Figure 8.7 depicts the optode placement relative to the international 10-20 system.[90,91] To couple the fibers to the head, we used a flexible plastic spine as the substrate to which

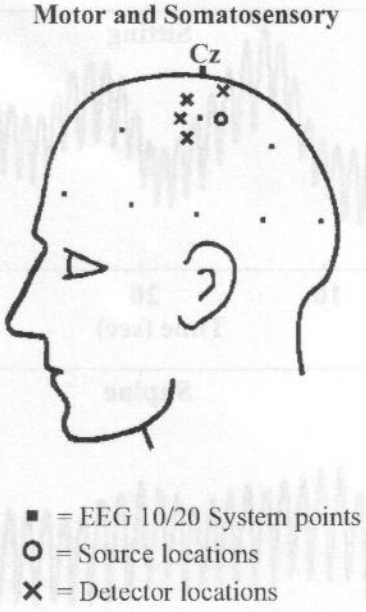

FIGURE 8.7 Diagram showing the placement of the light source (o) and four photo detectors (x) for the NIRS measurements.

we attached the fibers. Side-firing fiber bundles (3-mm core diameter) were developed to maintain a low profile on the scalp and to minimize motion artifact. Simple SMA connectors achieved coupling of the sources and detectors to the instrument. Figure 8.5 shows an image of the setup with the cap attached to a head-phantom.

At the start of the experiment, the subject remained seated in a chair while the cap was put on. No gel or special hair treatment was required except to wiggle the fibers through the hairs to improve the contact with the skin. The first subject was simply asked to close his eyes and relax during two 40-sec recording periods. For the first period, the subject sat upright in a chair; for the second, the subject was asked to lie supine. The purpose of these two recordings was to see what physiological variables could be recorded by the instrument in a simple resting baseline condition. Another subject in the supine position was asked to perform a four-finger flexion and extension task. The task was to flex and extend the four fingers of a designated hand for 15-sec blocks, alternated with 15-sec periods of rest, paced at 3 Hz by visual stimuli on a computer monitor. Signals were recorded continuously for 315-sec runs (10 active periods, 11 resting periods) from the region surrounding C3 and C4 (international 10-20 system designations).

Data acquisition for the DOT experiments was similar. The subject was first fitted with the optical cap (fibers again attached to a plastic substrate, anchored to a well-secured headband), and positioned supine. Again, visual stimuli paced the four-finger flexion and extension task, with optical recordings beginning 30 sec prior to the onset of stimuli.

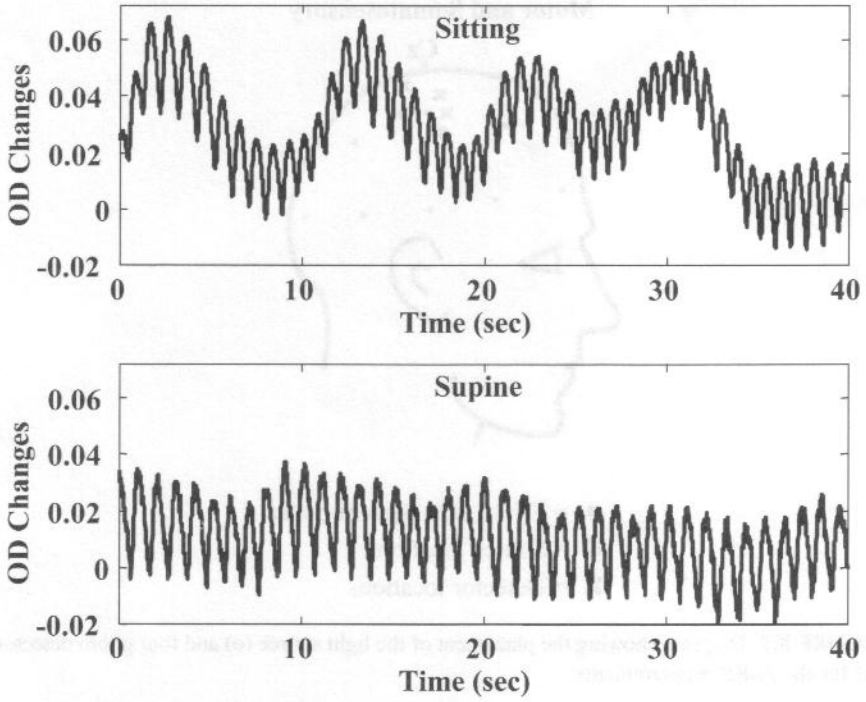

FIGURE 8.8 Results from 40 sec of recording during an eyes-closed resting condition in a subject while in a sitting position (top) and supine (bottom). Optical density changes observed from the 830-nm laser are shown. In both traces, heart pulsations are clearly evident. In the sitting case, a second, high-amplitude periodicity of ~0.1 Hz is also evident, while it is essentially absent in the supine position (see text).

8.4.2 NIRS Results

8.4.2.1 Brain Recording Experiments

Baseline Recording: Figure 8.8 shows the observed amplitude modulations from a single subject during two different baseline conditions (in optical density units). The top trace — with data gathered at 830 nm from approximately location C3 in the international 10-20 system — shows 40 sec of eyes-closed baseline while the subject was seated upright. The bottom trace is from the same subject, again eyes-closed baseline, but while lying supine. Heart pulsations are clear in both records, while in the upright case an additional high-amplitude oscillation of ~0.1 Hz appears. The frequency of this periodicity corresponds to the Mayer wave — a systemic blood pressure oscillation more prominent when standing or sitting than when lying down.[92,93] Further investigation is needed to fully characterize this signal and verify its source.

Motor Task: The data gathered from a single detector (again sampling from approximately location C3) for the motor task appear in Figure 8.9 for a supine subject. The horizontal bar indicates the period of motor activity, while the upper

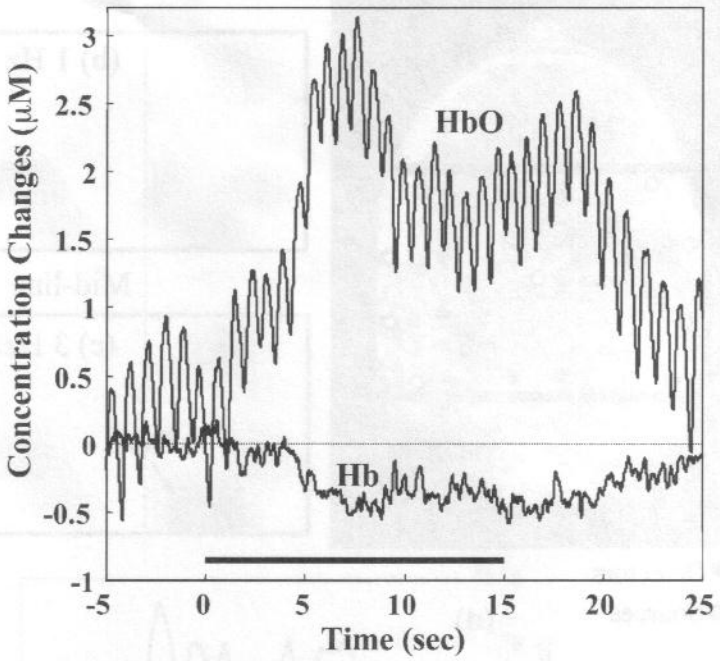

FIGURE 8.9 Changes in oxyhemoglobin (HbO) and deoxyhemoglobin (Hb) beneath C3 in a single subject while performing right-hand, four-finger flexions and extensions at approximately 3 Hz (horizontal bar). Concentration changes were calculated from raw optical data via the MBLL. No averaging was required due to the large activation amplitude typically associated with motor tasks.

and lower traces show the change in HbO and Hb (respectively) from the rest period. These traces involve no averaging, only a boxcar smoothing function with a 2-Hz bandwidth. The expected hemodynamic response for this task, based on previous fMRI experiments, would be an increase in HbO (and concomitant decrease in Hb) starting ~3 sec after motor activity onset, peaking around 6 to 9 sec post-onset, and decaying to baseline some 7 to 11 sec following the cessation of motor activity.[94] Both optical time courses match this profile. Also noteworthy is that the MBLL, Equation 8.4, has segregated the pulsatile changes in the optical signal more or less exclusively to the HbO signal,[93] and the activity-induced change in this signal is approximately a factor of 4 larger in magnitude than the observed change in Hb. For the MBLL analysis we assumed that the differential pathlength factor was equal to 6 at each wavelength.

8.4.3 Imaging Result

For the DOT experiment, the arrangement of the 9 sources and 12 detectors spanning the subject's left and right hemispheres is shown in Figure 8.10a. Fifteen seconds of rest data were collected, followed by 8 blocks of 15 sec of right-finger extension and flexion and 15 sec of rest. This 255-sec run was repeated twice: once with visual

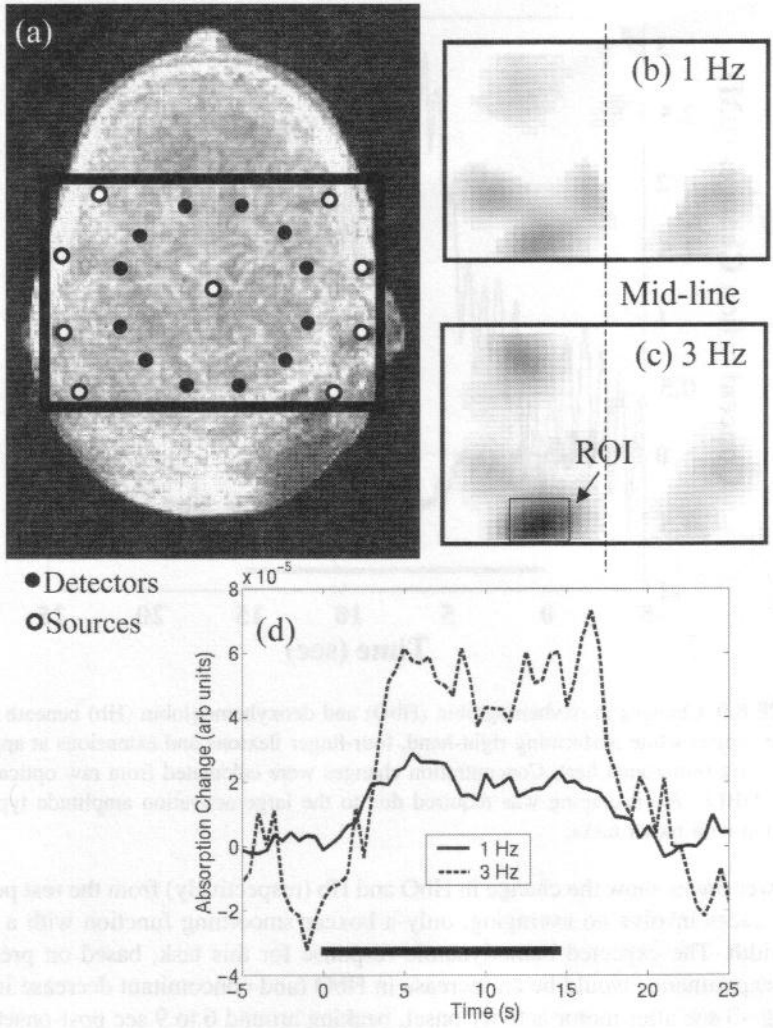

FIGURE 8.10 Images of motor activation obtained with a continuous-wave diffuse optical tomography system with 9 sources and 12 detectors (a). The images reconstructed at 785 nm for a 1- and 3-Hz finger flexion and extension are shown in (b) and (c). (d) shows the time course of the absorption change in the region-of-interest (ROI) shown in (c).

cues guiding a 1-Hz extension and flexion, and once with 3 Hz. Images were reconstructed in a single plane with Tikhonov regularization, using a regularization parameter of $\alpha = 0.8$, assuming that the head was flat and spatially uniform (i.e., semi-infinite homogeneous space) and that the activation occurred in a single plane 2 cm deep in the brain. The assumption of activation in a single plane will project all activity above and below it into the plane, causing image artifacts. Likewise, the assumption of a flat head will introduce model errors, resulting in image artifacts.

For these reasons, the images are considered qualitative and preliminary, as the magnitude of the errors introduced by the assumptions is as yet unexplored.

The images reconstructed from the block averaged data from 1- and 3-Hz stimulation are shown in Figure 8.10b and c, respectively. These images show absorption changes at 785 nm at the end of the stimulation block prior to signal recovery to baseline. The observed spatial patterns are qualitatively similar, with stronger amplitude modulation in the 3-Hz image. Based on the anatomical MRI, the posterior activations roughly correspond to primary sensorimotor cortex and show a typical pattern of stronger activation on the left (contralateral to movement) than on the right (ipsilateral) side. The left anterior activation corresponds roughly to premotor cortex (Brodmann area 6) and shows less lateralization, in keeping with the more bilateral interconnectivity of premotor cortex. In Figure 8.10d we show the time course of the absorption change at 785 nm in response to activation in the region of interest indicated in Figure 8.10c. As is expected for functional activation, the onset of the absorption change is delayed by 2 to 3 sec and time-to-peak is between 5 and 9 sec. Furthermore, the amplitude is observed to be a factor of 3 greater at 3 Hz than at 1 Hz.

At this stage the data are too preliminary to extract oxy- and deoxyhemoglobin concentration changes from the signal. Confidence in the imaged concentrations will come with further development and validation of the methodology, in particular with a better understanding of the image reconstruction accuracy. Our initial exploration of the image accuracy indicates that the presented measurement geometry is too sparse for obtaining accurate image magnitudes (and thus concentrations) with the present reconstruction algorithms. Accuracy can be improved with a denser measurement geometry or improved reconstruction algorithms.

8.5 FUTURE DIRECTIONS

Given the relative immaturity of DOT as an imaging modality, a broad spectrum of future directions remains open to inquiry. At one end of the spectrum lies the important theoretical work on light diffusion through inhomogeneous media and improved methods for 3D-image reconstruction. Such work will help improve the spatial and quantitative nature of the data obtainable from DOT. At the other end of the spectrum lie the clinical applications such as monitoring patients for signs of stroke or low oxygen saturation, especially in a bedside setting. In between the theoretical and clinical realms lies the ground of our most recent efforts. This work involves validation and comparision of DOT with other imaging modalities (e.g., EEG and fMRI) and, more importantly, the synergy generated by simultaneous application of two or more brain-monitoring technologies.

8.5.1 Quantitative Accuracy

On the theoretical side, the Modified Beer–Lambert Law (MBLL), discussed earlier, is a common method for calculating Hb and HbO concentrations from optical signals, with known pitfalls. Implementation of this model requires a value for the differential

pathlength factor (DPF) for each wavelength (Equation 8.3). The DPF is simply a scaling factor transforming the source–detector separation into a measure of the average path length that each wavelength of light takes through the tissue from source to detector. While the DPF can be measured by using FD and TD optical systems,[95-98] the complexity and cost of such systems often prohibits DPF measurement for each subject prior to functional recording. When using a CW system, one has to rely on previously tabulated DPF values.[95,99-101] This approach suffers from uncertainties in the DPF, which varies between people and tissue types[95] and with age.[99] Alternatively, one can calibrate the DPF against the cardiac-induced arterial pulsation,[93] but this requires an accurate measurement of the cardiac pulsation within the optical signal, which is not always achievable. The greatest concern with using the MBLL is that it assumes that changes in the hemoglobin concentrations are spatially uniform over the measurement sampling volume.

During functional brain imaging, however, changes in optical properties result from localized changes in the blood oxygenation and blood volume within the brain; that is, the changes are not uniform over the measurement sampling volume. This is most clearly understood by considering the geometry involved in noninvasive measurements. In an adult human, the first layer of tissue is 0.5 to 1 cm of scalp, followed by 0.5 to 1 cm of skull, followed by a thin layer (0 to 2 mm) of cerebral spinal fluid and, finally, the gray and white matter of the brain. Functional activation changes occur primarily in the cortex, the outermost layer of the brain, and are therefore up to 2 cm below the source and detector. Thus, light traveling from the source to the detector will at best encounter the functional change over only a very small portion of the optical sampling volume, even for a spatially large activation. Such local changes violate the MBLL assumption of a global change and thereby introduce an error reminiscent of partial volume averaging.

With fMRI, for example, the signal from a given voxel is a weighted average of all the changes occurring within that voxel. Because of this, a 50% signal change restricted, for example, to half of the voxel will produce a 25% change in fMRI signal for that voxel. It is clear that this type of error will always produce an underestimate of the signal change when the change is assumed to be global to the sampling volume (as is done with the MBLL analysis). Similarly, a functional change in Hb and HbO concentrations within the optical sampling volume will be underestimated when the change is assumed to be global but is actually focal in nature. Furthermore, if the partial volume effect is different for each wavelength, it could lead to cross-talk in the determination of oxy- and deoxyhemoglobin concentration changes.[32]

The cross-talk produced by the differential wavelength partial volume effect needs further investigation to better understand the significance of the error in interpretation of optical signals. For instance, anecdotal evidence suggests that cross-talk can be significant when using 785 and 830 nm but less significant when using 760 and 830 nm. The difference may arise from the differing sensitivity that each wavelength pair has to the change in oxygen saturation of the hemoglobin. In addition, better models can be employed for analyzing the experimental data. These models would attempt to consider the focal nature of the hemodynamic change when analyzing the data, as is done by DOT.

8.5.2 MRI–DOT Synergy

As we have discussed, DOT has the potential to provide quantitative measures of deoxyhemoglobin (Hb) as well as oxyhemoglobin (HbO), provided partial volume errors can be minimized. If the tissue anatomy is known, then DOT will have an easier job determining the optical properties of the different structures and characterizing any regional activation. The anatomical data obtainable via MRI can provide just such data, resulting in a synergetic relationship between MRI and DOT.[101-103]

To see how this synergy develops, consider the following sequence of events. First, we acquire anatomical MRI scans that (1) help localize our optical probes with respect to the underlying brain anatomy and (2) can be used to segment the head into a variety of tissue types (typically air, scalp, skull, cerebral spinal fluid, and white and gray matter). The segmented head can then be used for Monte Carlo studies in photon diffusion to determine the DOT instrument's sensitivity to various tissue types and depths. The functional MRI data, once processed to provide functional maps, can also provide an estimate of the spatial extent and magnitude of the hemodynamic changes due to functional challenge.

These estimates can, of course, be used to compare the functional sensitivity of DOT with fMRI. More importantly, however, these estimates can also be used as a model of optical changes that would allow more accurate quantitation of the Hb and HbO changes during functional challenge. This way, simultaneous MRI and CW-DOT recordings have the potential to provide more accurate spatial localization of an activation and absolute quantitation of the Hb and HbO changes found there — something impossible with either technique alone.

A first step toward merging MRI and DOT is to examine simultaneously acquired fMRI and NIRS time courses from spatially co-registered locations. Figure 8.11 shows an example of this comparison for a single subject performing the unimanual motor task described earlier. The fMRI signal is showing a percent change in the deoxyhemoglobin concentration (positive percent represents a decrease in concentration of unknown absolute magnitude). The NIRS signal, on the other hand, shows the relative concentration changes in oxy- and deoxyhemoglobin. Qualitatively, the signals are similar.

The next step toward combining MRI and DOT is to examine spatial correspondences in the diffuse optical image and the fMRI, completing an analysis of the spatial–temporal correlation of the two methods. One can then proceed to use the anatomical information provided by the MRI to obtain more accurate estimates of where the light has sampled within the head, using the Monte Carlo method described earlier. With these better estimates of the photon migration sensitivity profile, one can expect to obtain a more accurate characterization of the spatially varying optical properties within the medium.

This synergy work is still at a very early stage. Although further developments and computational refinements are definitely necessary, this approach promises to provide accurate, quantitative measures of Hb and HbO changes in brain tissue — something heretofore lacking from both imaging modalities. Combining this quantitative information with the spatial detail of simultaneously acquired fMRI will

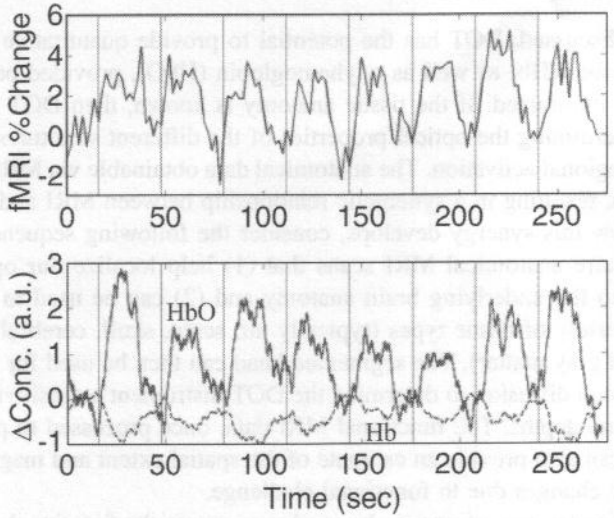

FIGURE 8.11 Time series plots for a subject performing the 3-Hz, right-hand, four-finger flexion and extension. Top: the fMRI signal averaged across all significantly activated pixels within contralateral (left) primary motor cortex. Vertical bars indicate the onset of motor activity; offset occurred 15 sec later. Bottom: NIRS signals from the optode sampling the region closest to the significant fMRI activation region, time-locked with the fMRI signal. The top curve shows changes in [HbO], in arbitrary units (a.u.), and the bottom curve shows changes in [Hb].

result in a more complete and accurate picture of the hemodynamic changes and a better understanding of the brain's response to functional challenge.

8.5.3 Imaging Newborn Babies

In a more clinical domain, Hintz et al.[104] have demonstrated that DOT can be used bedside in the neonatal intensive care unit to measure brain activation in response to passive motor stimulus. An illustrative result of their work with an earlier version of our DOT imaging system is reproduced in Figure 8.12. For the study presented in this figure, the patient was a 33-week estimated gestational age infant. The infant was quiet and asleep but not pharmacologically sedated or paralyzed. The patient had normal heart rate and O_2 saturation by pulse oximetry during the approximately 40-min study period. The probe used for this study was 3×6 cm and was placed in true midline position in the area that corresponded to the motor cortex. Baseline data were collected for 20 sec, at which point the patient's right arm was flexed and extended at the elbow. The data for each image were collected over a 5-sec interval. Data were collected at 780 and 830 nm.

As seen on the second row of images, there are clear increases in absorbance seen at 830 nm, indicated by the increase in yellow to red color, but also, as seen in the first row of images, much greater absorbance at 780 nm. Taken together, these data indicate an increase in blood flow to the imaged area but an overall increase

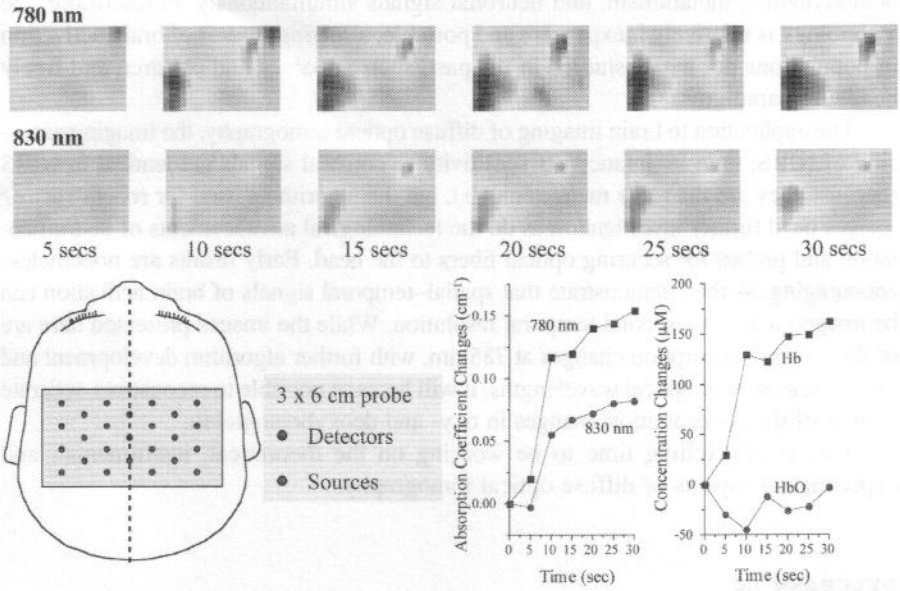

FIGURE 8.12 Time-series images at 780 and 830 nm presented every 5 sec following onset of a passive motor-sensory task whereby the baby's right arm is flexed ~30° once a second for 30 sec. Darker area indicates increased absorption. A greater absorption increase is seen at 780 than at 830 nm. The arrangement of the nine sources at each of the two wavelengths and the 16 detectors is shown as the overlay on a drawing on the baby's head. The probe spans the left and right hemispheres. The time course of the absorption change in focal activation in the contralateral hemisphere is shown, along with the corresponding changes in hemoglobin concentrations.

in deoxyhemoglobin concentration, as well. A graphic representation of the greater absorbance at 780 vs. 830 nm is seen in Figure 8.12, along with the indicated increase in deoxyhemoglobin.

This work demonstrates the feasibility of using DOT for imaging brain activation in the infant brain. This same technology can be equally applied to young children. Both of these populations have traditionally been difficult to study with any other neuroimaging methods because of extreme sensitivity to motion artifacts. DOT is less sensitive to motion artifacts for two main reasons: 1) as opposed to EEG, DOT is not as sensitive to muscular activity and 2) the DOT imaging probe can be made lightweight and moves with the subject's head.

8.6 SUMMARY

The rapidly growing literature from the past ten years clearly demonstrates the ability of near-infrared spectroscopy to noninvasively measure cerebral hemodynamic changes in response to stimuli. Furthermore, the literature is growing in support of the unique ability of NIRS to measure metabolic (cytochrome oxidase) and neuronal (fast optical scattering changes) signals. NIRS is unique as a neuromonitoring and neuroimaging technique because it is the only method that can potentially measure

hemodynamic, metabolism, and neuronal signals simultaneously. Furthermore, the technology is relatively inexpensive and portable, allowing studies of brain activation in populations not easily studied in the past, such as babies and children and freely behaving paradigms.

The application to brain imaging of diffuse optical tomography, the imaging extension of NIRS, is in its infancy. Its sensitivity to cerebral signals is identical to NIRS (because they are the same measurements), but the algorithms used for reconstructing images need further investigation as do the technological advancements of instrumentation and probes for securing optical fibers to the head. Early results are nonetheless encouraging, as they demonstrate that spatial–temporal signals of brain activation can be imaged with a subsecond temporal resolution. While the images presented here are of the intrinsic absorption changes at 785 nm, with further algorithm development and careful selection of optical wavelengths, it will become possible to reconstruct accurate images of the concentration changes in oxy- and deoxyhemoglobin.

This is an exciting time to be working on the theoretical, instrumental, and experimental aspects of diffuse optical tomography.

REFERENCES

1. Jobsis, F.F., Noninvasive infrared monitoring of cerebral and myocardial sufficiency and circulatory parameters, *Science*, 198, 1264, 1977.
2. Arridge, S.R., Optical tomography in medical imaging, *Inverse Probl.*, 15, R41, 1999.
3. Chance, B. et al., Comparison of time-resolved and unresolved measurements of deoxyhemoglobin in brain, *Proc. Natl. Acad. Sci. U.S.A.*, 85, 4971, 1988.
4. Chance, B., Optical method, *Annu. Rev. Biophys. Chem.*, 20, 1, 1991.
5. Cope, M. and Delpy, D.T., System for long-term measurement of cerebral blood flow and tissue oxygenation on newborn infants by infrared transillumination, *Med. Biol. Eng. Comput.*, 26, 289, 1988.
6. Wray, S., Cope, M., and Delpy, D.T., Characteristics of the near infrared absorption spectra of cytochrome aa3 and hemoglobin for the noninvasive monitoring of cerebral oxygenation, *Biochim. Biophys Acta*, 933, 184, 1988.
7. McCormick, P.W. et al., Noninvasive cerebral optical spectroscopy for monitoring cerebral oxygen delivery and hemodynamics, *Clin. Care Med.*, 19, 89, 1991.
8. Benaron, D.W. et al., Noninvasive methods for estimating *in vivo* oxigenation, *Clin. Pediatr.*, 31, 258, 1992.
9. Elwell, C.E. et al., Quantification of adult cerebral hemodynamics by near-infrared spectroscopy, *J. Appl. Physiol.*, 77, 2753, 1994.
10. Belliveau, J.W. et al., Functional mapping of the human visual cortex by magnetic resonance imaging, *Science*, 254, 716, 1991.
11. Kwong, K.K. et al., Dynamic magnetic resonance imaging of human brain activity during primary sensory stimulation, *Proc. Natl. Acad. Sci. U.S.A.*, 89, 5675, 1992.
12. Ogawa, S. et al., Intrinsic signal changes accompanying sensory stimulation: functional brain mapping with magnetic resonance imaging, *Proc. Natl. Acad. Sci. U.S.A.*, 89, 5951, 1992.
13. Frahm, J. et al., Dynamic MR imaging of human brain oxygenation during rest and photonic stimulation, *J. Magn. Reson. Imaging*, 2, 501, 1992.

14. Bandettini, P.A. et al., Time course EPI of human brain function during task activation, *Magn. Reson. Med.*, 25, 390, 1992.
15. Hoshi, Y. and Tamura, M., Detection of dynamic changes in cerebral oxygenation coupled to neuronal function during mental work in man, *Neurosci. Lett.*, 150, 5, 1993.
16. Villringer, A. et al., Near infrared spectroscopy (NIRS): a new tool to study hemodynamic changes during activation of brain function in human adults, *Neurosci. Lett.*, 154, 101, 1993.
17. Okada, F. et al., Gender- and handedness-related differences of forebrain oxygenation and hemodynamics, *Brain Res.*, 601, 337, 1993.
18. Chance, B. et al., Cognitive activated low frequency modulation of light absorption in human brain, *Proc. Natl. Acad. Sci. U.S.A.*, 90, 2660, 1993.
19. Villringer, A. and Chance, B., Non-invasive optical spectroscopy and imaging of human brain function, *Trends Neurosci.*, 20, 435, 1997.
20. Prichard, J.W. and Rosen, B.R., Functional study of the brain by NMR, *J. Cerebr. Blood Flow Metab.*, 14, 365, 1994.
21. Meek, J.H. et al., Regional changes in cerebral haemodynamics as a result of a visual stimulus measured by near infrared spectroscopy, *Proc. R. Soc. London B*, 261, 351, 1995.
22. Hock, C. et al., Age dependency of changes in cerebral hemoglobin oxygenation during brain activation: a near infrared spectroscopy study, *J. Cerebr. Blood Flow Metab.*, 15, 1103, 1995.
23. Gratton, G. et al., Rapid changes of optical parameters in the human brain during a tapping task, *Neuroscience*, 7, 446, 1995.
24. Maki, A. et al., Spatial and temporal analysis of human motor activity using noninvasive NIR topography, *Med. Phys.*, 22, 1997, 1995.
25. Heekeren, H.R. et al., Cerebral haemoglobin oxygenation during sustained visual stimulation — a near-infrared spectroscopy study, *Philos. Trans. R. Soc. Lond. B Biol. Sci.*, 352, 743, 1997.
26. Obrig, H. and Villringer, A., Near-infrared spectroscopy in functional activation studies. Can NIRS demonstrate cortical activation? *Adv. Exp. Med. Biol.*, 413, 113, 1997.
27. Hoshi, Y. and Tamura, M., Near-infrared optical detection of sequential brain activation in the prefrontal cortex during mental tasks, *NeuroImage*, 5, 292, 1997.
28. Colier, W.N. et al., Human motor-cortex oxygenation changes induced by cyclic coupled movements of hand and foot, *Exp. Brain. Res.*, 129, 457, 1999.
29. Toronov, V. et al., Near infrared study of fluctuation in cerebral hemodynamics during rest and motor stimulation: temporal analysis and spatial mapping, *Med. Phys.*, 27, 801, 2000.
30. Franceschini, M.A. et al., On-line optical imaging of the human brain with 160-ms temporal resolution, *Optics Express*, 6, 49, 2000.
31. Benaron, D.A. et al., Noninvasive functional imaging of human brain using light, *J. Cerebr. Blood Flow Metab.*, 20, 469, 2000.
32. Boas, D.A. et al., The accuracy of near infrared spectroscopy and imaging during focal changes in cerebral hemodynamics, *NeuroImage*, 13, 76, 2001.
33. Colier, W.N. et al., Simultaneous near-infrared spectroscopy monitoring of left and right occipital areas reveals contra-lateral hemodynamic changes upon hemi-field paradigm, *Vision Res.*, 41, 97, 2001.
34. Jobsis, F.F., Noninvasive, infrared monitoring of cerebral and myocardial oxygen sufficiency and circulatory parameters, *Science*, 198, 1264, 1977.

35. Wyatt, J.S. et al., Quantification of cerebral oxygenation and haemodynamics in sick newborn infants by near infrared spectrophotometry, *Lancet*, ii, 1063, 1986.
36. Chance, B. and Williams, G.R., The respiratory chain and oxidative phosphorylation, *Adv. Enzimol.*, 17, 65, 1956.
37. Lockwood, A.H. et al., Effects of acetazolamide and electrical stimulation on cerebral oxidative metabolism as indicated by cytochrome oxidase redox state, *Brain Res.*, 308, 9, 1984.
38. Wong Riley, M.T., Cytochrome oxidase: an endogenous metabolic marker for neuronal activity, *Trends Neurosci.*, 12, 94, 1989.
39. Kohl, M. et al., Changes in cytochrome-oxidase oxidation in the occipital cortex during visual stimulation: Improvement in sensitivity by the determination of the wavelength dependence of the differental pathlength factor, *Proc. SPIE*, 3194, 18, 1998.
40. Wobst, P. et al., Linear aspects of changes in deoxygenated hemoglobin concentration and cytochrome oxidase oxidation during brain activation, *NeuroImage*, 13, 520, 2001.
41. Salzberg, B.M. and Obaid, A.L., Optical studies of the secretory event at vertebrate nerve terminals, *Exp. Biol.*, 139, 195, 1988.
42. Stepnoski, R.A. et al., Noninvasive detection of changes in membrane potential in cultured neurons by light scattering, *Proc. Natl. Acad. Sci. U.S.A.*, 88, 9382, 1991.
43. Rector, D.M., Rogers, R.F., and George, J.S., A focusing image probe for assessing neural activity *in vivo*, *J. Neurosci. Methods*, 91, 135, 1999.
44. Gratton, G. et al., Shades of gray matter: noninvasive optical images of human brain responses during visual stimulation, *Psychophysiology*, 32, 505, 1995.
45. Gratton, G. et al., Toward non-invasive 3-D imaging of the time course of cortical activity: investigation of the depth of the event-related optical signal (EROS), *NeuroImage*, 11, 491, 2000.
46. Steinbrink, J. et al., Somatosensory evoked fast optical intensity changes detected non-invasively in the adult human head, *Neurosci. Lett.*, 291, 105, 2000.
47. Hebden, J.C., Arridge, S.R., and Delpy, D.T., Optical imaging in medicine: I. Experimental techniques, *Phys. Med. Biol.*, 42, 825, 1997.
48. Cope, M., *The Development of a Near-Infrared Spectroscopy System and Its Application for Noninvasive Monitoring of Cerebral Blood and Tissue Oxygenation in the Newborn Infant*, University College London, 1991.
49. Delpy, D.T. et al., Estimation of optical pathlength through tissue from direct time of flight measurement, *Phys. Med. Biol.*, 33, 1433, 1988.
50. Matcher, S.J. et al., Performance comparison of several published tissue near-infrared spectroscopy algorithms, *Anal. Biochem.*, 227, 54, 1995.
51. Ishimaru, A., *Wave Propagation and Scattering in Random Media*, Academic Press, San Diego, 1978.
52. Patterson, M.S., Chance, B., and Wilson, B.C., Time resolved reflectance and transmittance for the non-invasive measurement of tissue optical properties, *Appl. Optics*, 28, 2331, 1989.
53. Haskell, R.C. et al., Boundary conditions for the diffusion equation in radiative transfer, *J. Opt. Soc. Am. A*, 11, 2727, 1994.
54. Furutsu, K. and Yamada, Y., Diffusion approximation for a dissipative random medium and the applications, *Phys. Rev. E*, 50, 3634, 1994.
55. Durduran, T. et al., Does the photon diffusion coefficient depend on absorption? *J. Opt. Soc. Am. A*, 14, 3358, 1997.

56. Farrell, T.J., Patterson, M.S., and Wilson, B., A diffusion theory model of spatially resolved, steady state diffuse reflectance for the noninvasive determination of tissue optical properties *in vivo, Med. Phys.*, 19, 879, 1992.
57. Jackson, J.D., *Classical Electrodynamics*, 2nd ed., John Wiley & Sons, New York, 1975.
58. Kak, A.C. and Slaney, M., *Principles of Computerized Tomographic Imaging*, IEEE Press, New York, 1988.
59. Arridge, S.R. and Hebden, J.C., Optical imaging in medicine: II. Modelling and reconstruction, *Phys. Med. Biol.*, 42, 841, 1997.
60. Wang, L., Jacques, S.L., and Zheng, L., MCML — Monte Carlo modeling of light transport in multi-layered tissues, *Comput. Methods Programs Biomed.*, 47, 131, 1995.
61. Firbank, M. et al., An investigation of light transport through scattering bodies with non-scattering regions, *Phys. Med. Biol.*, 41, 767, 1996.
62. Okada, E. et al., Theoretical and experimental investigation of near-infrared light propagation in a model of the adult head, *Appl. Optics*, 36, 21, 1997.
63. Dale, A.M., Fischl, B., and Sereno, M.I., Cortical surface-based analysis. I. Segmentation and surface reconstruction, *NeuroImage*, 9, 179, 1999.
64. Benaron, D.A. and Stevenson, D.K., Optical time-of-flight and absorbance imaging of biologic media, *Science*, 259, 1463, 1993.
65. Chance, B. et al., Comparison of time-resolved and unresolved measurements of deoxyhemoglobin in brain, *Proc. Natl. Acad. Sci. U.S.A.*, 85, 4971, 1988.
66. Cubeddu, R. et al., Time-resolved imaging on a realistic tissue phantom: μs' and μa images vs. time-integrated images, *Appl. Opt.*, 35, 4533, 1996.
67. Grosenick, D., Wabnitz, H., and Rinneberg, H., Time-resolved imaging of solid phantoms for optical mammography, *Appl. Optics*, 36, 221, 1997.
68. Gratton, E. et al., Measurements of scattering and absorption changes in muscle and brain, *Philos. Trans. R. Soc. Lond. B Biol. Sci.*, 352, 727, 1997.
69. Jiang, H. et al., Simultaneous reconstruction of optical absorption and scattering maps in turbid media from near-infrared frequency-domain data, *Opt. Lett.*, 20, 2128, 1995.
70. Pogue, B.W. and Patterson, M.S., Frequency-domain optical-absorption spectroscopy of finite tissue volumes using diffusion-theory, *Phys. Med. Biol.*, 39, 1157, 1994.
71. Pogue, B.W. et al., Instrumentation and design of a frequency-domain diffuse optical tomography imager for breast cancer detection, *Optics Express*, 1, 391, 1997.
72. Chance, B. et al., Phase measurement of light absorption and scattering in human tissues, *Rev. Sci. Instru.*, 689, 3457, 1998.
73. Nioka, S., Luo, Q., and Chance, B., Human brain functional imaging with reflectance CWS, *Adv. Exp. Med. Biol.*, 428, 237, 1997.
74. Siegel, A.M., Marota, J.J.A., and Boas, D.A., Design and evaluation of a continuous-wave diffuse optical tomography system, *Optics Express*, 4, 287, 1999.
75. Maki, A. et al., Visualizing human motor activity by using non-invasive optical topography, *Front Med. Biol. Eng.*, 7, 285, 1996.
76. Colier, W. et al., A new and highly sensitive optical brain imager with 50 Hz sample rate, *NeuroImage*, 11, 542, 2000.
77. Hebden, J.C., Evaluating the spatial resolution performance of a time-resolved optical imaging system, *Med. Phys.*, 19, 1081, 1992.
78. Ntziachristos, V. et al., Multichannel photon counting instrument for spatially resolved near infrared spectroscopy, *Rev. Sci. Instrum.*, 70, 193, 1999.

79. Arridge, S.R. and Lionheart, W.R.B., Nonuniqueness in diffusion-based optical tomography, *Optics Lett.*, 23, 882, 1998.
80. Colier, W.N.J.M. et al., Age dependency of cerebral oxygenation assessed with near infrared spectroscopy, *J. Biomed. Optics*, 2, 162, 1997.
81. Colier, W.N. et al., Human motor-cortex oxygenation changes induced by cyclic coupled movements of hand and foot, *Exp. Brain Res.*, 129, 457, 1999.
82. Takahashi, K. et al., Activation of the visual cortex imaged by 24-channel near-infrared spectroscopy, *J. Biomed. Opt.*, 5, 93, 2000.
83. Schmitz, C.H. et al., Instrumentation and calibration protocol for imaging dynamic features in dense-scattering media by optical tomography, *Appl. Optics*, 39, 6466, 2000.
84. Quaresima, V. et al., Noninvasive measurement of cerebral hemoglobin oxygen saturation using two near infrared spectroscopy approaches, *J. Biomed. Opt.*, 5, 201, 2000.
85. A.N.S., *American National Standard for Safe Use of Lasers*, ANSI Z136.1-1993, American National Standards Institute, New York, New York, 1993.
86. Bandettini, P.A. et al., Processing strategies for time-course data sets in functional MRI of the human brain, *Magn. Reson. Med.*, 30, 161, 1993.
87. Belliveau, J.W. et al., Functional mapping of the human visual cortex by magnetic resonance imaging, *Science*, 254, 716, 1991.
88. Halgren, E. et al., Location of human face-selective cortex with respect to retinotopic areas, *Hum. Brain Map.*, 7, 29, 1999.
89. Drummond, S.P. et al., Sleep deprivation-induced reduction in cortical functional response to serial subtraction (in process citation), *Neuroreport*, 10, 3745, 1999.
90. Jasper, H.H., The ten-twenty electrode system of the International Federation, *EEG Clin. Neurophysiol.*, 10, 371, 1958.
91. Klem, G.H. et al., The ten-twenty electrode system of the International Federation. The International Federation of Clinical Neurophysiology, *Electroencephalogr. Clin. Neurophysiol. Suppl.*, 52, 3, 1999.
92. Taylor, J.A. et al., Low-frequency arterial pressure fluctuations do not reflect sympathetic outflow: gender and age differences, *Am. J. Physiol.*, 274, H1194, 1998.
93. Kohl, M. et al., Determination of the wavelength dependence of the differential pathlength factor from near-infrared pulse signals, *Phys. Med. Biol.*, 43, 1771, 1998.
94. Bandettini, P.A. et al., Time course EPI of human brain function during task activation, *Magn. Reson. Med.*, 25, 390, 1992.
95. Duncan, A. et al., Optical pathlength measurements on adult head, calf and forearm and the head of the newborn infant using phase resolved optical spectroscopy, *Phys. Med. Biol.*, 40, 295, 1995.
96. van der Zee, P. et al., Experimentally measured optical pathlengths for the adult's head, calf and forearm and the head of the newborn infant as a function of interoptode spacing, *Adv. Exp. Med. Biol.*, 316, 143, 1992.
97. Fantini, S. et al., Non-invasive optical imaging of the piglet brain in real time, *Optics Express*, 4, 308, 1999.
98. Franceschini, M.A., Gratton, E., and Fantini, S., Non-invasive optical method to measure tissue and arterial saturation: an application to absolute pulse oximetry of the brain, *Opt. Lett.*, 24, 829, 1999.
99. Duncan, A. et al., Measurement of cranial optical path length as a function of age using phase resolved near infrared spectroscopy, *Pediatr. Res.*, 39, 889, 1996.

100. Essenpreis, M. et al., Wavelength dependence of the differential pathlength factor and the log slope in time-resolved tissue spectroscopy, *Adv. Exp. Med. Biol.*, 333, 9, 1993.
101. Barbour, R.L. et al., MRI-guided optical tomography:prospects and computation for a new imaging method, *IEEE Computation Sci. Eng.*, 2, 63, 1995.
102. Pogue, B.W. and Paulsen, K.D., High-resolution near-infrared tomographic imaging simulations of the rat cranium by use of a priori magnetic resonance imaging structural information, *Optics Lett.*, 23, 1716, 1998.
103. Ntziachristos, V. et al., Concurrent MRI and diffuse optical tomography of breast after indocyanine green enhancement, *Proc. Natl. Acad. Sci. U.S.A.*, 97, 2767, 2000.
104. Hintz, S.R. et al., Bedside functional imaging of a premature infant during passive motor activation, *J. Perinat. Med.*, 29, 335, 2001.